Supplementary Information

Nanoscale interfacial engineering enables highly stable and efficient perovskite photovoltaics

Anurag Krishna[1†*], Hong Zhang[2†], Zhiwen Zhou[2†], Thibaut Gallet[3], Mathias Dankl[4], Olivier Ouellette[2], Felix T. Eickemeyer[2], Fan Fu[6], Sandy Sanchez[2], Mounir Mensi[7], Shaik M. Zakeeruddin[2], Ursula Rothlisberger[4], G. N. Manjunatha Reddy[5], Alex Redinger[3], Michael Grätzel[2], Anders Hagfeldt[1‡*]

[1]Laboratory of Photomolecular Science, Institute of Chemical Sciences and Engineering, École Polytechnique Fédérale de Lausanne, Lausanne 1015, Switzerland.

[2]Laboratory of Photonics and Interfaces, École Polytechnique Fédérale de Lausanne, Lausanne 1015, Switzerland.

[3]Scanning Probe Microscopy Laboratory, Department of Physics and Materials Science, University of Luxembourg, Luxembourg.

[4]Laboratory of Computational Chemistry and Biochemistry, École Polytechnique Fédérale de Lausanne, Lausanne 1015, Switzerland.

[5]Univ. Lille, CNRS, Centrale Lille Institut, Univ. Artois, UMR 8181-UCCS-Unité de Catalyse et Chimie du Solide, F-59000 Lille, France

[6]Laboratory for Thin Films and Photovoltaics, Empa-Swiss Federal Laboratories for Materials Science and Technology, Überlandstrasse 129, CH-8600 Dübendorf, Switzerland.

[7]Institute of Chemical Sciences and Engineering, École Polytechnique Fédérale de Lausanne, Valais Wallis, CH-1951 Sion, Switzerland.

‡Present address: Department of Chemistry – Ångström Laboratory, Uppsala University, 75120 Uppsala, Sweden.

*Correspondence to: anurag.krishna@epfl.ch (A.K.); anders.hagfeldt@uu.se (A.H.)

†These authors contribute equally to this work.

This PDF file includes:

- Experimental Details
- Figs. S1 to S27
- Supplementary Note 1
- Tables S1-S3

Experimental Details

Materials. Fluorine-doped tin oxide (FTO) (10 Ω/sq) conductive glass was purchased from Nippon Sheet Glass (NSG). 2,5 thiophene dicarboxylic acid, 4-*tert*-butyl pyridine (TBP), lithium bistrifluorosulfonylimide (LiTFSI), acetonitrile (ACN), acetyl acetone, titanium diisopropoxide bis(acetylacetonate) 75 wt.% in isopropanol, and methylammonium chloride (MACl) were purchased from Sigma-Aldrich. Lead iodide (PbI_2) was purchased from Alfa Aesar. Formamidinium iodide (FAI) and titanium dioxide paste (TiO_2-30 NRD) were purchased from Greatcell. 2,2',7,7'-Tetrakis[*N*,*N*-di(4-methoxyphenyl)amino]-9,9'-spirobifluorene (Spiro-OMeTAD) was purchased from Xi'an Polymer Light Technology Corp. Methylammonium lead tribromide ($MAPbBr_3$) was purchased from Share Chem. Ultra-dry dimethylformamide (DMF), dimethyl sulfoxide (DMSO), ethanol (EtOH), and chlorobenzene (CB) were purchased from Acros. All the chemicals were used as received without further purification.

Preparation of perovskite precursor solution. For $(FAPbI_3)_{1-x}(MAPbBr_3)_x$ precursor solution preparation, a mixture of PbI_2 (755 mg), FAI (258 mg), MABr (6 mg), $PbBr_2$ (17 mg) and MACl (40 mg) was dissolved in 1 mL mixed solution of DMF and DMSO (volume ration of DMF/DMSO of 8:1).

Device fabrication: Fluoride-doped tin oxide glass substrates (FTO, 4.0 mm-thick, 10 Ω/sq, Nippon Sheet Glass) were patterned using zinc powder and concentrated hydrochloric acid (1 M). The patterned FTO was sequentially cleaned by 2 % commercial detergent (Hellmanex) water solution, deionized water, ethanol, and acetone in an ultrasonic bath for 15 min, rinsed with deionized water, and then dried by air blowgun. After O_3/ultraviolet treatment for 15 min, the 20-40 nm compact layer TiO_2 (c-TiO_2) was deposited on a cleaned FTO substrate by spray pyrolysis at 450 °C using a precursor solution of titanium diisopropoxide bis(acetylacetonate) with oxygen as the carrier gas. The precursor solution was prepared by taking 75 wt.% diisopropoxide bis(acetylacetonate) in isopropanol, diluting with ethanol with a volume ratio of 1:9, and addition of 4 vol% acetylacetone. After cooling down to room temperature and O_3/ultraviolet treatment for 15 min, the mesoporous TiO_2 (mp-TiO_2) was spin-coated at 4000 rpm for 20 s onto the c-TiO_2 using a commercial paste (Dyesol 30 NR-D) diluted in ethanol (1:6, weight ratio) to achieve 100 to 150 nm thickness. After drying at 80 °C for 10 min, the TiO_2 films were gradually sintered to 450 °C, kept at this temperature for 30 min, and cooled to room temperature. Before use, the films were treated with 0.1 M solution of Li-TFSI in acetonitrile by spin coating at 3000 rpm for 20 s and then were sintered at 450 °C for 30 min. After cooling down to 150 °C, the substrates were transferred to a dry-air glovebox (relative humidity < 15%) for the deposition of perovskite films. The perovskite film was deposited onto the mp-TiO_2 substrate from a precursor, as described above. The precursor solution was spin-coated in a two-step process at 1000 rpm for 10 s and 6000 rpm for 25 s, respectively. During the second step, 500-600 µl of diethyl ether (Acros) was dropped on the spinning substrate 10 s prior to the end of the process. The substrates were sequentially heated at 150 °C for 10 min for perovskite crystal formation. For ligand treatment, the 2,5 thiophene dicarboxylic acid ligand powder was dissolved in isopropanol at 70 °C for 2 hours to form solutions with different concentration viz. 5mM, 10mM and 20mM. Then 60 µl of the ligand solution was dynamic spin-coated (in dynamic spin-coating the solution is put on the

spinning substrates) on to the as-formed perovskite films at 5500 rpm for 30 s. The treated perovskite films were heated at 100 °C for 5 min. A hole transport material solution containing 75 mM spiro-OMeTAD (>99.5%, Xi'an Polymer Light Technology Corp.) in chlorobenzene with 40 mM Li-TFSI (99.95%, Sigma-Aldrich) and 270 mM tBP (96%, Sigma-Aldrich) additives was dynamic spin-coated onto the substrate at 3000 rpm for 30 s. Finally, a gold electrode (~80 nm) was deposited by thermal evaporation.

XRD measurements. Thin-film X-ray diffraction (XRD) spectra were recorded on an X'Pert MPD PRO (PANanalytical) equipped with a ceramic tube providing Ni-filtered (Cu anode, λ =1.54060 Å) radiation and a RTMS X'Celerator (PANalytical).

SEM measurements. The morphologies of the films were characterized using a high-resolution scanning electron microscope (Zeiss Merlin) with an in-lens detector.

Solid-state NMR measurements. The spin-coated target films on glass substrates were scratched to obtain approximately 25 milligrams of the powder. This material was packed into a 3.2 mm rotor closed with Vespel® caps. All 1D ^{1}H MAS and 2D ^{1}H-^{1}H correlation NMR experiments were carried out on a Bruker Avance Neo (18.8 T, ^{1}H Larmor frequency = 800.13 MHz) spectrometer using a 3.2 mm H-X probe. The nutation frequency for ^{1}H was 192.3 kHz, corresponding to a 90° pulse duration of 1.3 µs. The MAS frequency was 20 kHz. The ^{1}H spin-lattice relaxation times (T_1) for protons sites in MA and FA+ cations were determined to be 34 s and 32 s, respectively, based on inversion recovery measurements and analyses. 1D ^{1}H MAS NMR spectrum was acquired using 284 co-added transients using a relaxation delay of 44 s, corresponding to a total experimental time of 3.5 h. A 2D ^{1}H-^{1}H double-quantum(DQ)-single-quantum (SQ) NMR spectrum was acquired using a Back-to-Back (BaBa) sequence[1]. The DQ coherences were excited using a rotor synchronized recoupling time of 50 µs, which corresponds to one rotor period ($1\tau_r$), and reconverted using a 16-step phase cycle to choose $\Delta p = \pm 2$ on the DQ excitation pulses (4 steps) and $\Delta p = \pm 1$ (4 steps), where p is the coherence order. A rotor-synchronized t_1 increment of 50 µs was applied to acquire the indirect ^{1}H DQ dimension with 128 t_1 increments, each with 16 co-added transients, corresponding to a total experimental time of 23 h. 2D ^{1}H-^{1}H spin diffusion NMR spectra were acquired using different mixing times, 50, 200, 500 and 1000 ms. Each 2D spectrum was acquired using 380 t_1 increments, each with 4 co-added transients. The ^{1}H chemical shifts were calibrated with respect to neat TMS using adamantane as an external reference (^{1}H resonance, 1.81 ppm).

Kelvin probe force microscopy and scanning tunneling microscopy and spectroscopy measurements. These were carried out in an Omicron VT ultra-high vacuum scanning probe microscopy apparatus with a base pressure in the low 10^{-11}mbar range. The laser wavelength was 830 nm, which is outside of the absorption range of the samples. KPFM measurements were performed in the dark with Pt-Ir covered Si cantilevers with a nominal resonance frequency of 75kHz. The acquisition was carried out in single-pass frequency modulation KPFM. All measurements were conducted with the voltage applied to the sample. We used highly oriented pyrolytic graphite to calibrate the tip work function prior and after the measurement on the perovskite absorber. STS measurements were carried out in the dark from -2.5V to 2.5V at a tunneling current setpoint of 250pA. A grid of 150 x 150 points were defined prior to the CITS maps.

XPS and UPS measurements. Surface properties of the control and target perovskite film were probed by XPS and UPS on an AXIS Supra (Kratos Analytical Ltd, UK), with respectively a monochromated Al kα x-ray ($h\nu$ = 1486.9 eV) source and a He-I UV source ($h\nu$ = 21.22 eV). Pass energy was set to 40eV for XPS and 10 eV for UPS measurements. The samples were electrically grounded through the FTO substrate.

PL mapping. PL mapping was carried on a Renishaw InVia microscope. PL was excited using a 532nm laser operated at 0.0001% of its nominal power (ca~40mW). Data were analyzed using custom made Matlab scripts.

PL, TRPL, and UV-Vis measurements. UV-Vis absorptions were measured using Varian Cary 500 spectrometer (Varian USA). Photoluminescence quantum yield (PLQY) was measured using an integrating sphere (Fluorolog, Horiba JobinYvon), an Andor Kymera 193i spectrograph, and a 660 nm continuous-wave laser (OBIS, Coherent) set at 1-Sun equivalent photon flux (1.1 μm beam full-width half-maximum, 632 μW); photoluminescence was collected at normal incidence using a 0.1 NA, 110 μm-diameter optical fiber. For the absolute spectral calibration of the PLQY measurement system, we used a radiometrically calibrated halogen lamp (HL-3 plus CAL from Ocean Optics). To check the correctness of the calibration, we measured PLQY of a dye solution of indocyanine green in DMSO in the same setup and measured PLQY values within 15% deviation from the literature values. The photoluminescence lifetime was measured via time-correlated single-photon counting (TCSPC) using a LifeSpec II (Edinburgh Instruments) fluorescence spectrometer with a picosecond pulsed diode laser (EPL-510, Edinburgh Instruments) at 510 nm wavelength, 85 ps pulse width and 4.5 nJ/cm^2 fluence.

Photovoltaic performance measurements. The perovskite solar cells were measured using a 300 W Xenon light source from Oriel. The spectral mismatch between AM 1.5G and the solar simulator was calibrated by a Schott K113 Tempax filter (Prazosopms G; as & Optik GmbH). A silicon photodiode was used as the light intensity calibrator for each measurement. A Keithley 2400 is used for the current-voltage scan by applying an external voltage bias and measuring the response current with a scan rate of 50 mV/s. An anti-reflection coating was used for the champion devices. The device area was 0.25 cm^2 (0.5 cm × 0.5 cm). The cells were masked with a black metal mask with an area of 0.16 cm^2. No preconditioning (e.g., bias and light soaking) was used for the photovoltaic measurement. External quantum efficiency (EQE) spectra were recorded with a commercial apparatus (Arkeo-Ariadne, Cicci Research s.r.l.) based on a 300 W Xenon lamp. For J-V measurements of the champion cell, the front glass/FTO was coated with an antireflection film.

Stability measurements. The stability data was acquired from MPP tracking of the unencapsulated devices under a continuous nitrogen flow at 40 °C. This was done under a white light-emitting diode lamp with biologic MPG2 potentiostat. The device area was masked to around 0.09 cm^2. The light intensity was around 100 mW cm^{-2}. Due to the spectral mismatch between the white LEDs and solar spectra, the LED light intensity was calibrated to match the J_{sc} of the standard AM1.5 G conditions. For thermal stability, the devices were stored on a hot plate at 85 °C in glove N_2 glove box. The devices were periodically taken out, and PCE was recorded by measuring them with a solar simulator.

TOF-SIMS measurements. Time-of-flight secondary ion mass spectrometry (TOF-SIMS) measurements were performed on a ToF-SIMS.5 instrument from IONTOF, Germany. Dual-beam depth profiles were acquired using a 25-keV Bi_3^+ primary ion beam with an ion current of 0.43 pA. A 1-keV Cs+ sputter beam with a current of 57.36 nA was used to remove material layer by layer in interlaced mode, from a raster area of 500 µm × 500 µm. Mass spectrometry was performed on an area of 100 µm × 100 µm in the centre of the sputter crater. 2D surface images were acquired over a 10 µm × 10 µm area (256 × 256 pixel raster, 1 shot/pixel) using a 25-keV Bi_3^+ primary ion beam with an ion current of 0.52 pA. 500 scans were performed, resulting typical measurement time of around 3200 s. The intensity of I^- ions is normalized to total ions counts, which is a ratio of $I(I^-)/I(total)$ for every pixel in the image. In both depth profiles and 2D imaging mode, negative ions were collected.

Computational methods

All computations were done on the DFT level of theory using Quantum ESPRESSO v6.6. Apart from variable-cell relaxations, all relaxation and single-point energy (SPE) computations were performed using the Perdew-Burke-Ernzerhof (PBE) functional with ultrasoft pseudopotentials from the pslibrary 1.0.0, a wavefunction cutoff of 60 Ry, a charge density cutoff of 480 Ry, Gaussian spreading of 0.005 Ry and the semiempirical Grimme 's DFT-D3 vdW correction. For the variable-cell relaxations PBEsol was applied. For geometry optimisations and SPE computations a 3x3x2 and 4x4x3 k-point grid was applied respectively. The relaxation procedure for the defect structures is done in multiple steps. Initially, a 2x2x7 supercell of pure $FAPbI_3$ (without defects) was relaxed, followed by introducing 41 Å of empty space along the z-direction, in order to enable the addition of 2,5 thiophenedicarboxylic acid onto the surface and minimizing interactions between the periodically repeated replicas in the z-direction. Different starting configurations of the organic molecule on the surface were generated and relaxed. The lowest energy configurations were selected for introducing defects at various sites close to the organic passivation molecule followed by another full relaxation. A final single point energy computation was done on the relaxed defect structures in order to compute the projected density of states (PDOS). For the PDOS computations, the projections were symmetrized and a Gaussian broadening of 0.001 Ry was applied. In order to allow a comparison of the density of states for the studied systems, a band alignment was performed using the largest peak from the PDOS of the 5d-orbitals of Pb.

<u>Supplementary Note 1</u> : Calculation of ΔE_F, $V_{oc,\,rad}$

To calculate ΔE_F we used the PLQY measurements and the following equation[2]:

$$\Delta E_F = q\,V_{oc,rad} + k_B T\,ln(PLQY) \quad (1)$$

where q is the elementary charge, $V_{oc,rad}$ is the radiative limit of V_{oc}, k_B the Boltzmann constant and T = 25 °C the sample temperature. $V_{oc,rad}$ is calculated by the equation[3]:

$$V_{oc,\,rad} = \frac{k_B T}{q} \ln\left(\frac{J_{sc}}{J_{rad,\,0}} + 1\right) \quad (2)$$

Here, J_{sc} is the measured photocurrent, $J_{rad,0} = q\int_0^\infty a(E)\,\Phi_{BB}(E)dE$ the dark emission current and $\Phi_{BB}(E) = \frac{1}{4\,\pi^2\,\hbar^3\,c^2}\frac{E^2}{\exp\left(E/(k_B\,T)\right) - 1}$ the differential photon flux of blackbody radiation. The absorptance a(E) is derived from the PL spectra $\Phi_{PL}(E)$ by applying the detailed balance principle[4,5]: $\Phi_{PL}(E) \propto a(E)\Phi_{BB}(E)$.

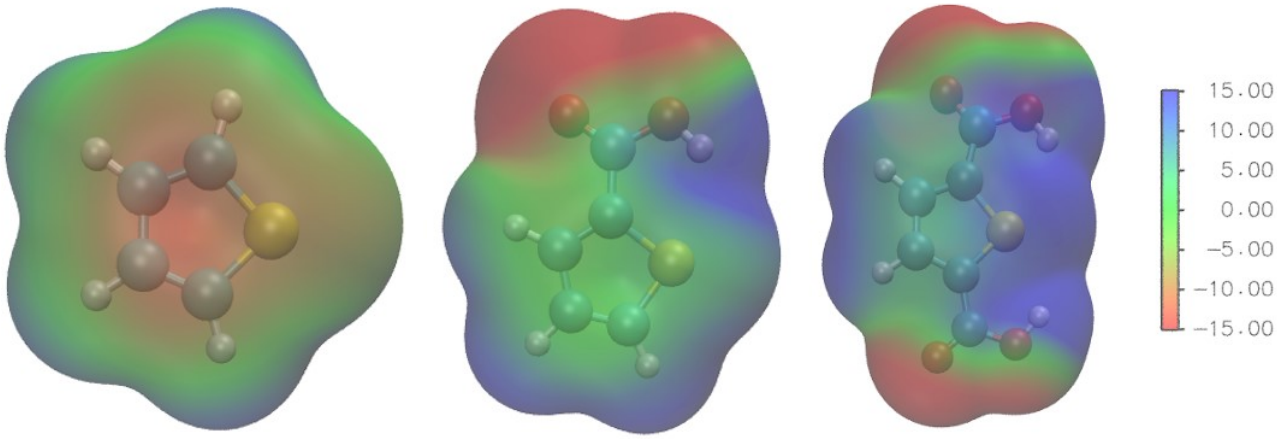

Fig. S1. Electrostatic potential (ESP) plots of thiophene, 2-thiophenecarboxylic acid and 2,5-thiophenedicarboxylic acid at the B3LYP/6-311++G(d,p) level of theory at an isosurface charge density value of 0.00202 e/Å^3.

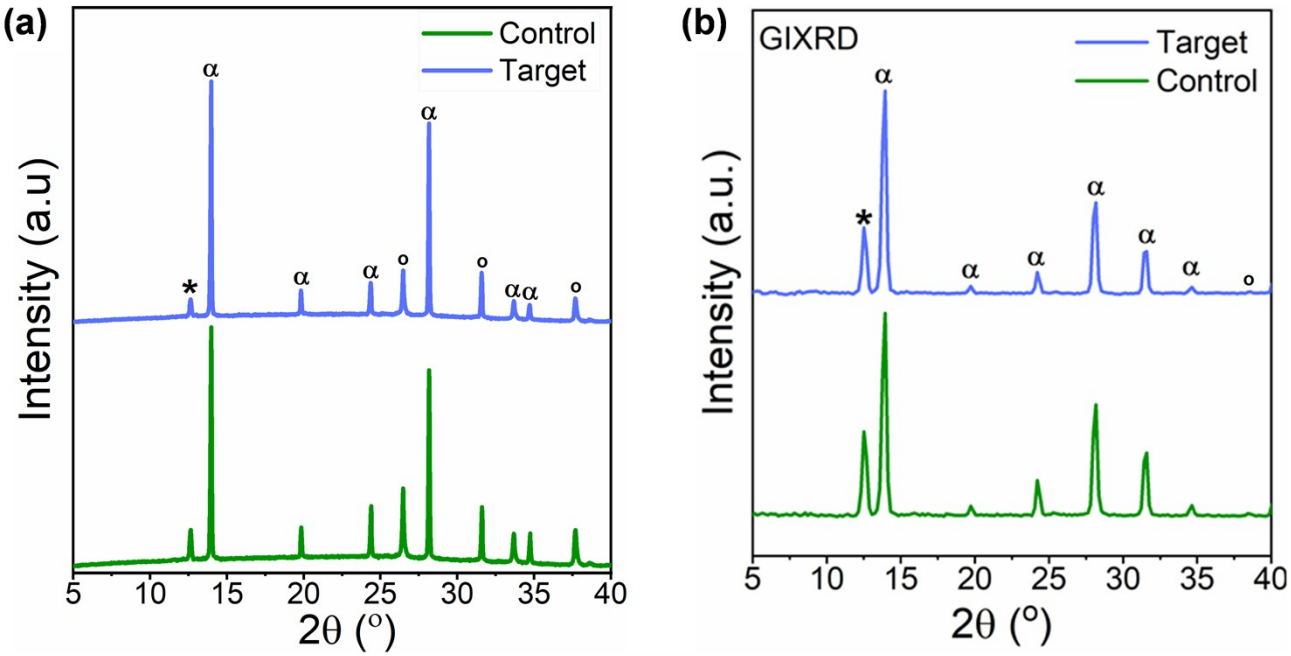

Fig. S2. (a) X-ray diffraction (XRD) and (b) GIXRD of the control and target films. α marks the 3D perovskite diffraction maxima, * corresponds to the PbI_2 diffraction peak and ° corresponds to diffraction peak from FTO.

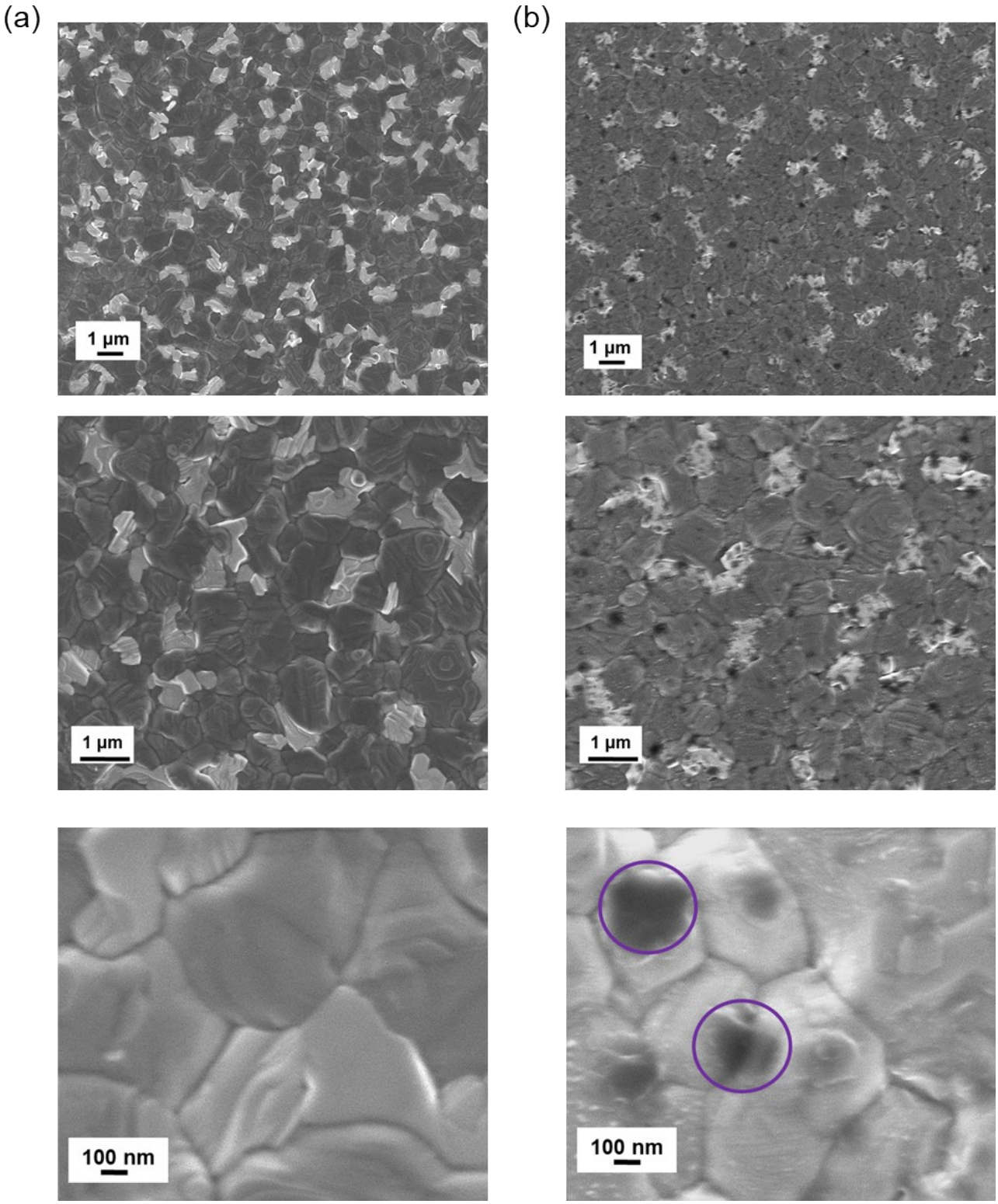

Fig. S3 Top-view high-resolution SEM images of (a) control and (b) target perovskite films, at different magnifications.

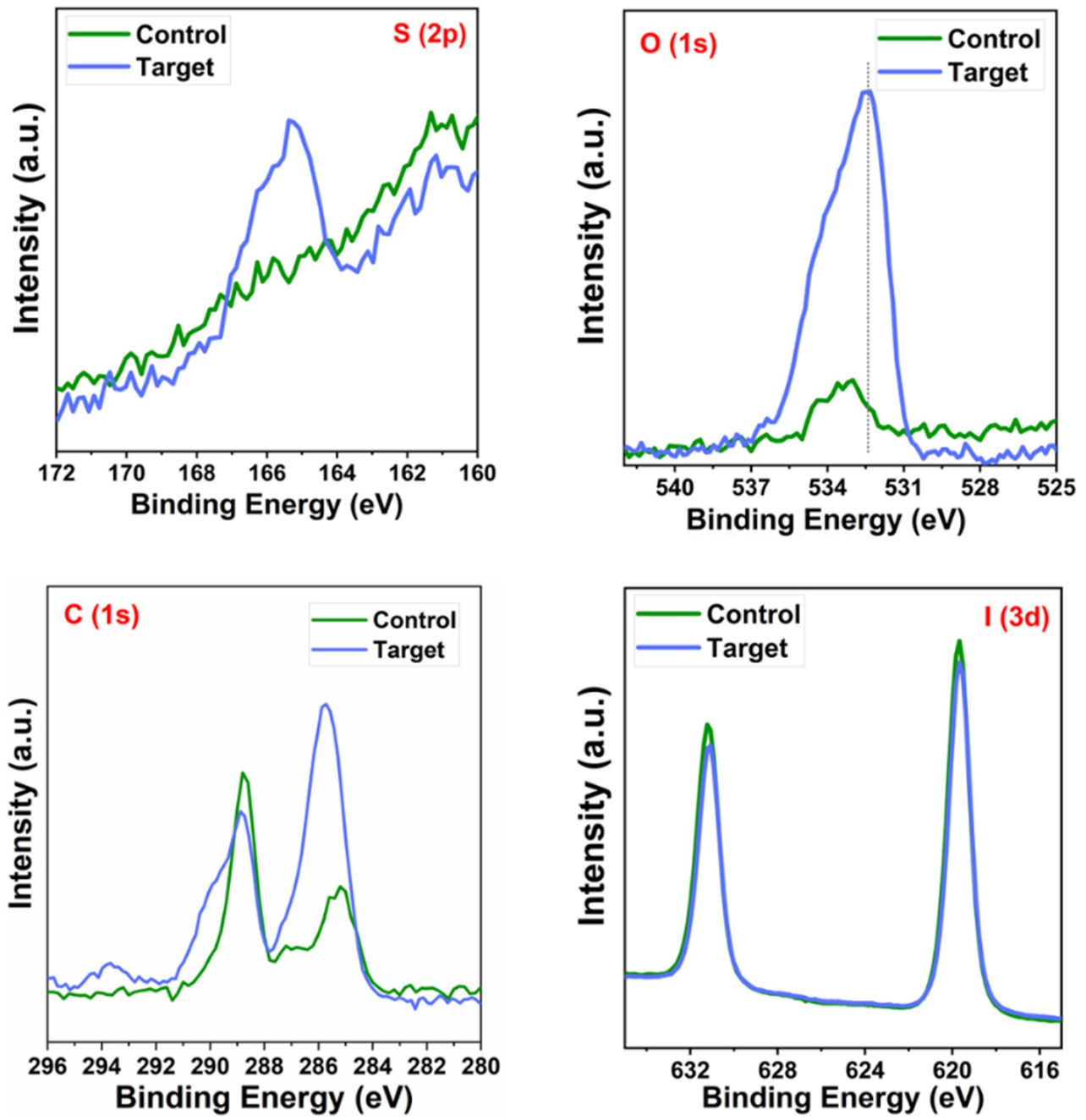

Fig. S4. X-ray photoelectron spectroscopy (XPS) core-level spectra of control and target perovskite film for S 2*p*, O 1*s*, C 1s and I 3*d*.

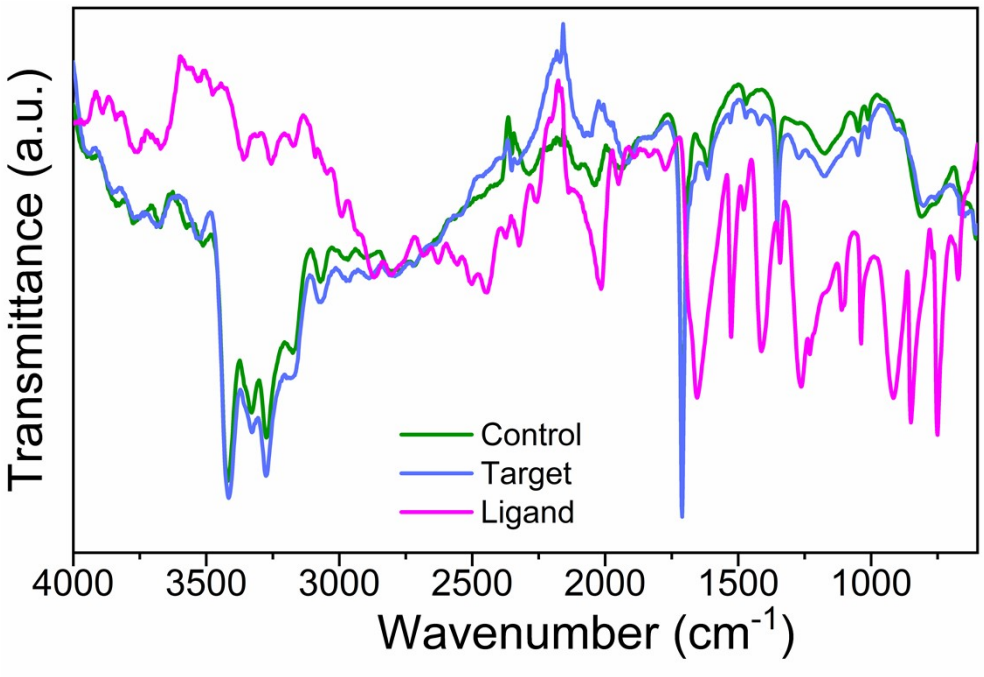

Fig. S5. Full FTIR spectra of the passivating agent, control, and target films.

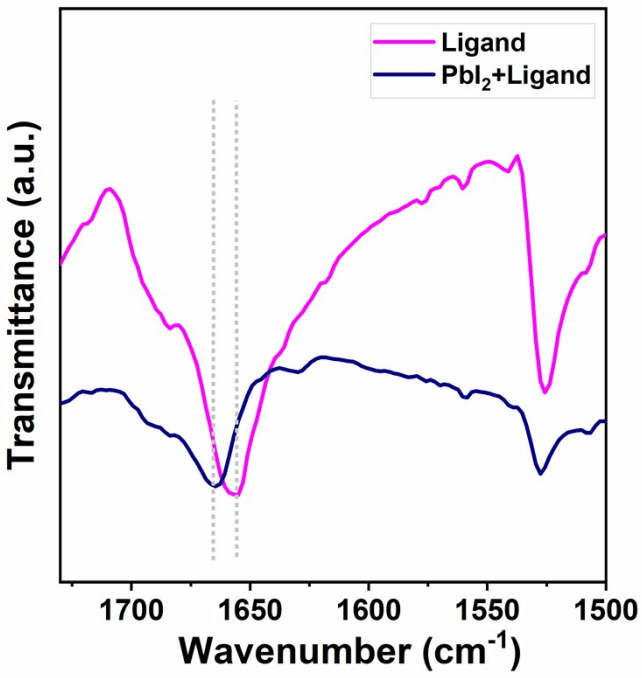

Fig. S6. Attenuated total reflection Fourier transform infrared (ATR-FTIR) spectra of pristine ligand, and lead iodide (PbI_2) with mixed with ligand.

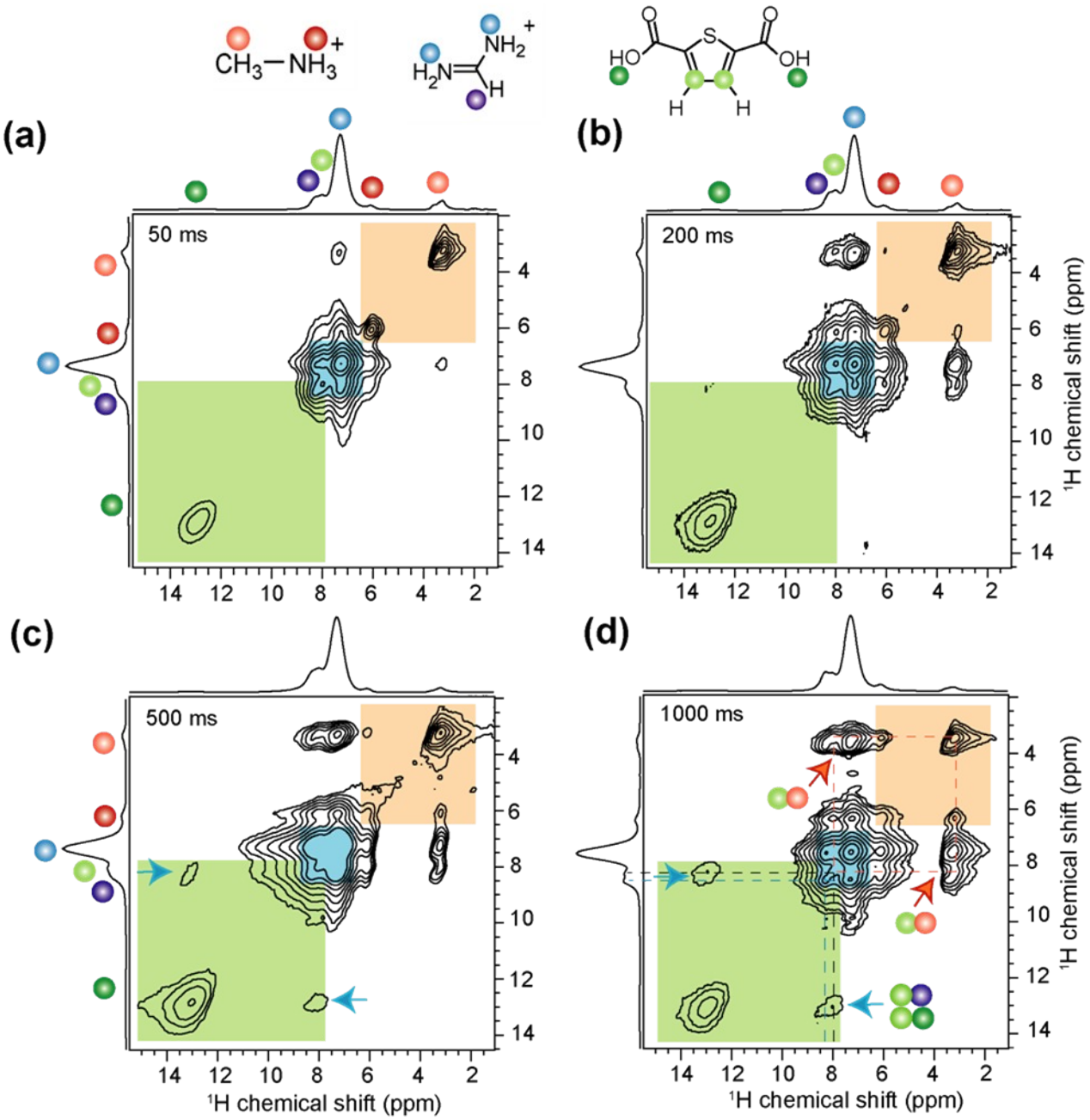

Fig. S7. Solid-state 2D ^{1}H-^{1}H correlation NMR spectra of target films acquired at 18.8 T (^{1}H, 800 MHz) and at room temperature with 20 kHz MAS using different spin diffusion times (a) 50 ms, (b) 200 ms, (c) 500 ms, and (d) 1000 ms. ^{1}H signals associated MA^{+}, FA^{+} and thiophene derivative are shown in color dots as depicted in the schematic structures (a). Red and blue arrows in (b) and (c) indicate the through-space ^{1}H-^{1}H proximities between surface passivating agent and MA^{+}/FA^{+} organic cations in perovskite crystals.

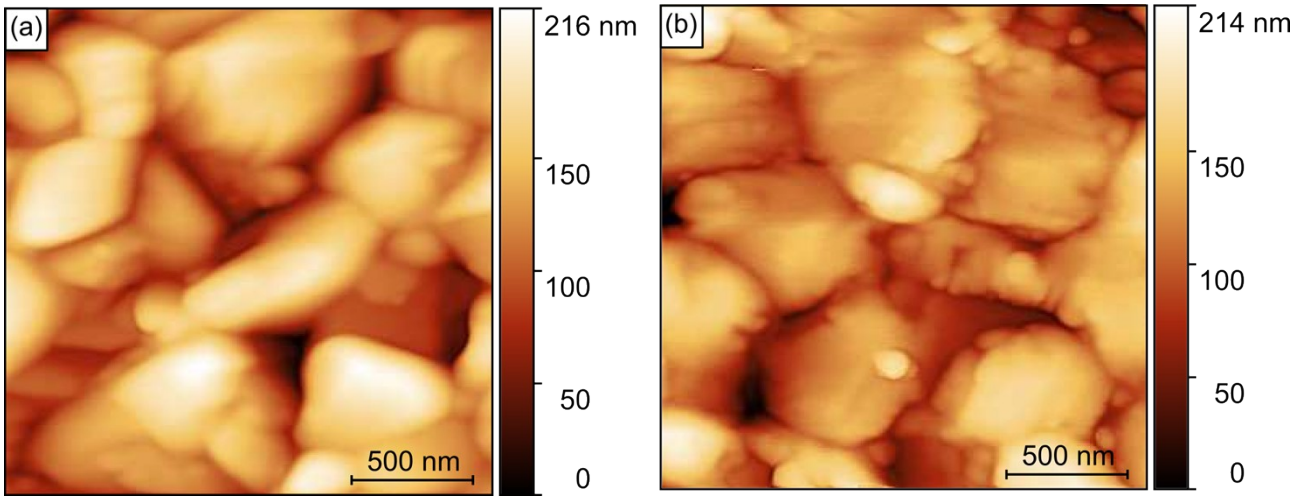

Fig. S8. Topography maps of (a) the control sample and (b) the target sample measured with atomic force microscopy.

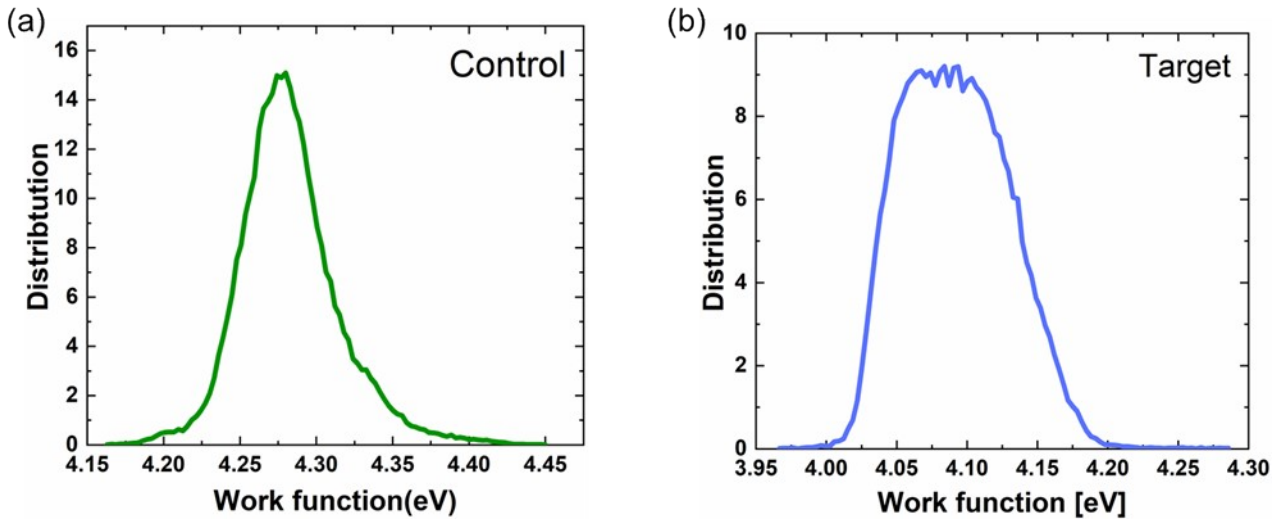

Fig. S9. Work function distribution of the (a) control and (b) Target.

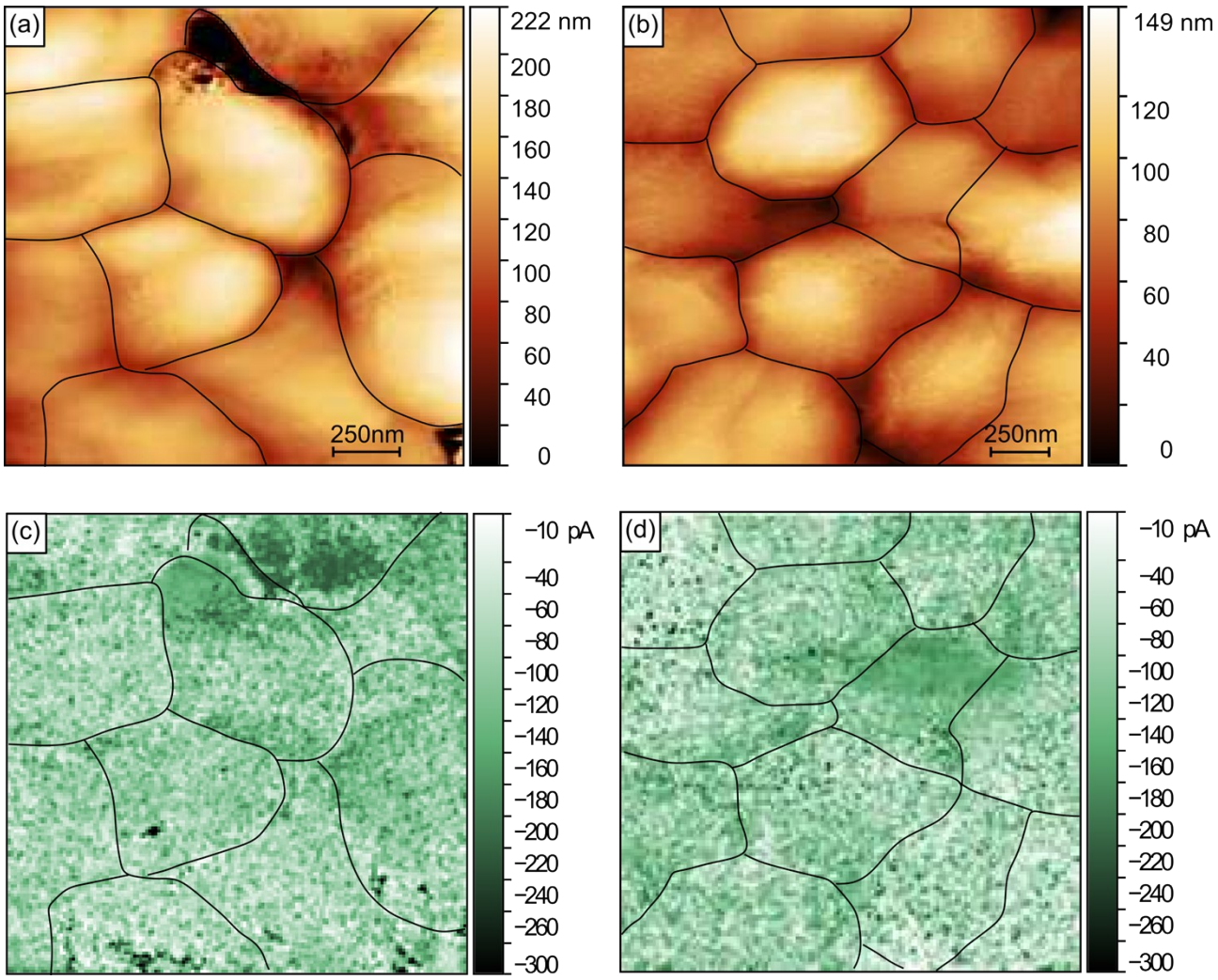

Fig. S10. Topography maps of (a) the control sample and (b) the target sample measured with scanning tunneling microscopy (c) and (d) are their respective conductance (dI/dV) maps at -2V. The lines drawn represent the grain boundaries to clearly distinct the different grains at the surface.

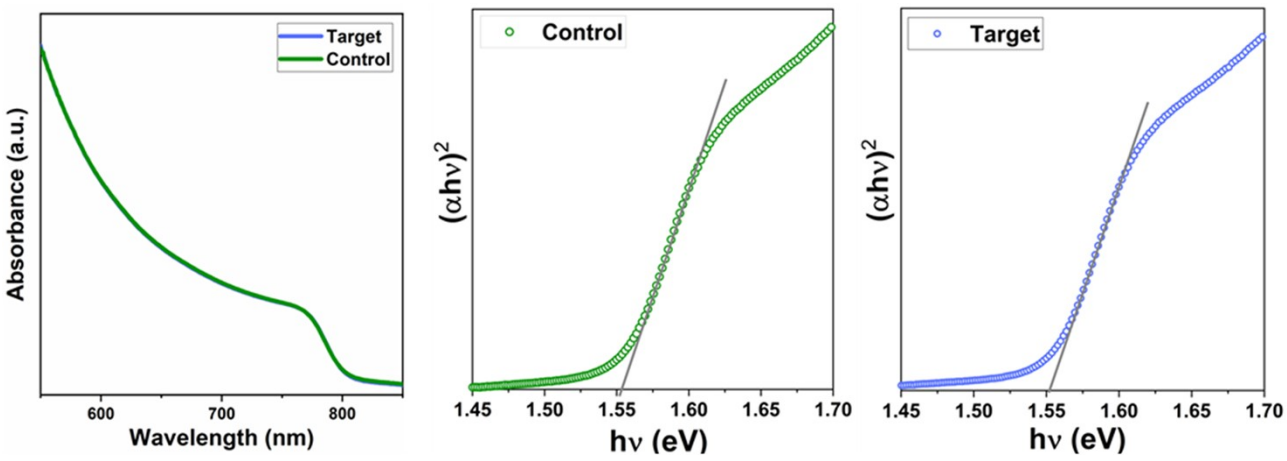

Fig. S11. UV-Vis spectra and the Tauc plot of the control and target films.

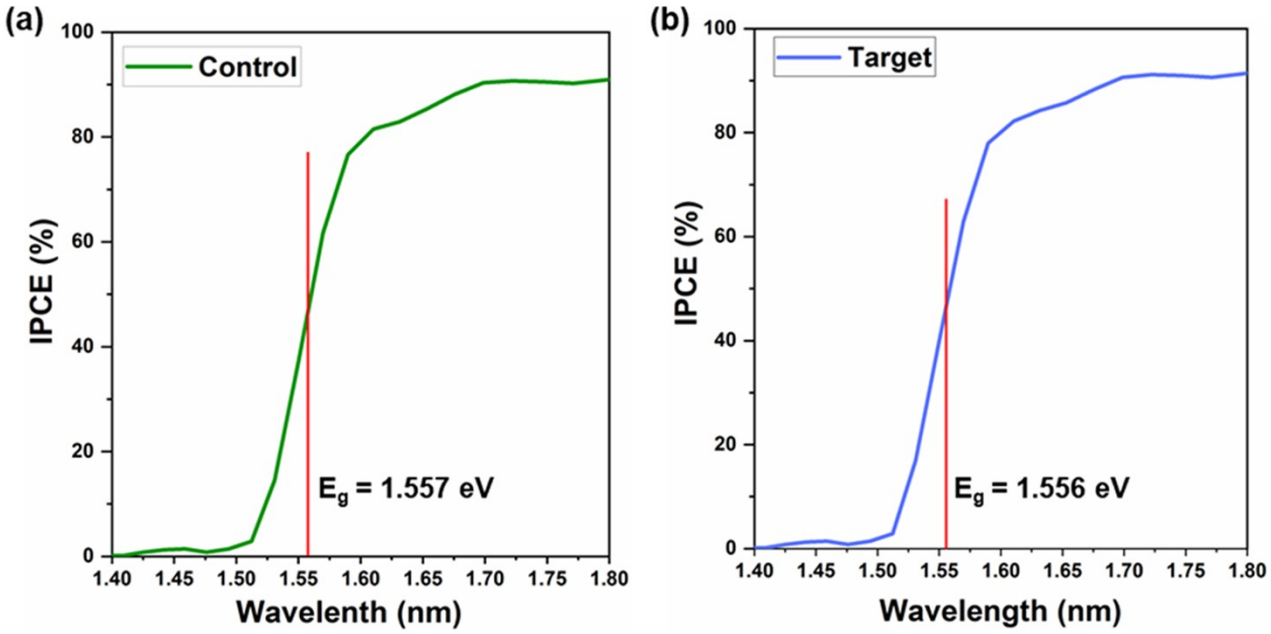

Fig. S12. The bandgap extracted from the inflection point of IPCE spectra of (a) control and (b) target.

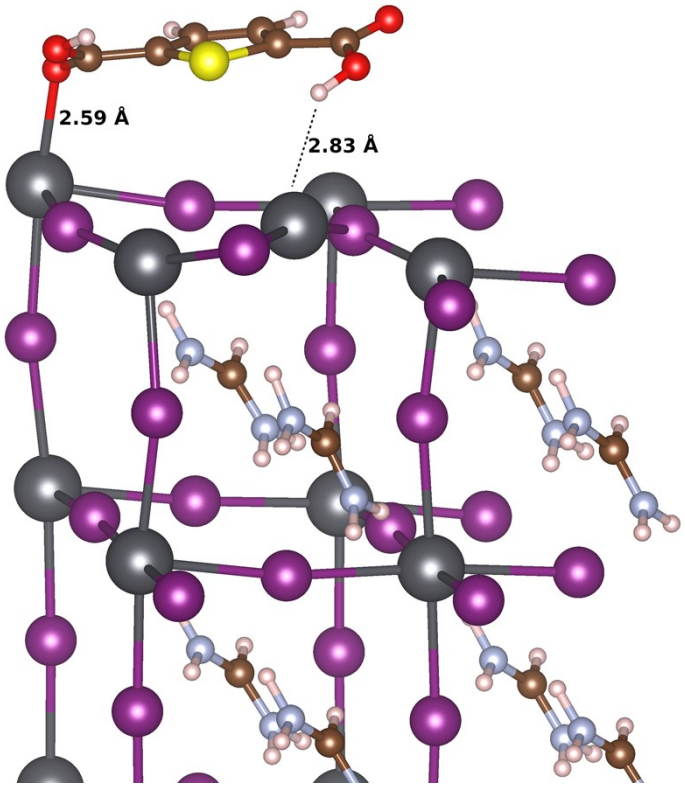

Fig. S13. The optimized configuration of the 2,5-thiophenedicarboxylic acid molecule on the surface of $FAPbI_3$ with Pb_I defect.

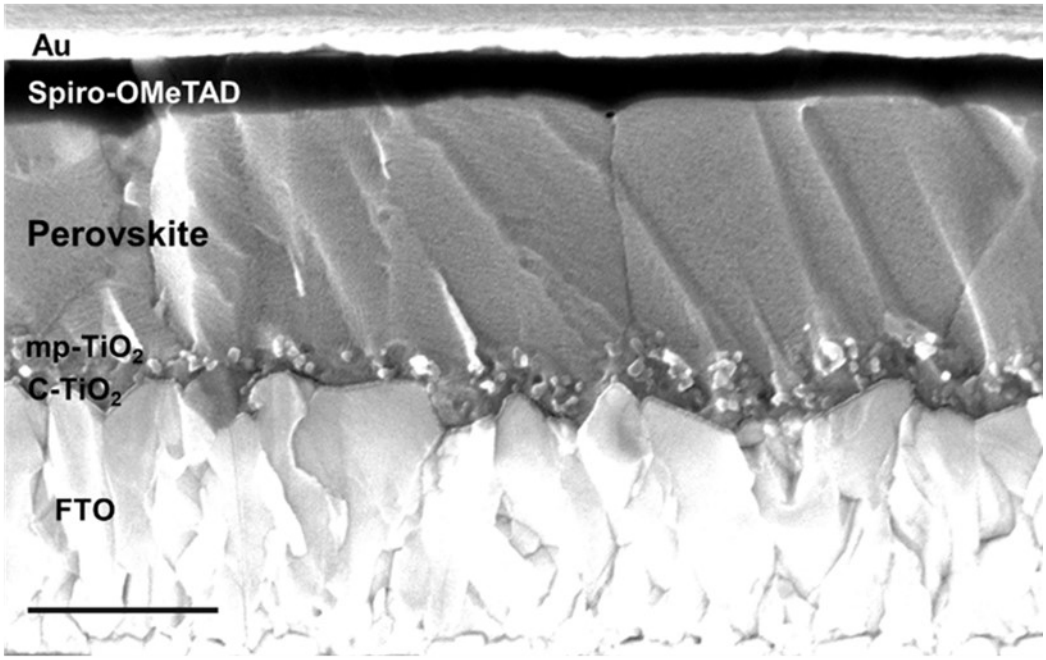

Fig. S14. Cross-sectional SEM image of the PSC. The scale bar is 500 nm.

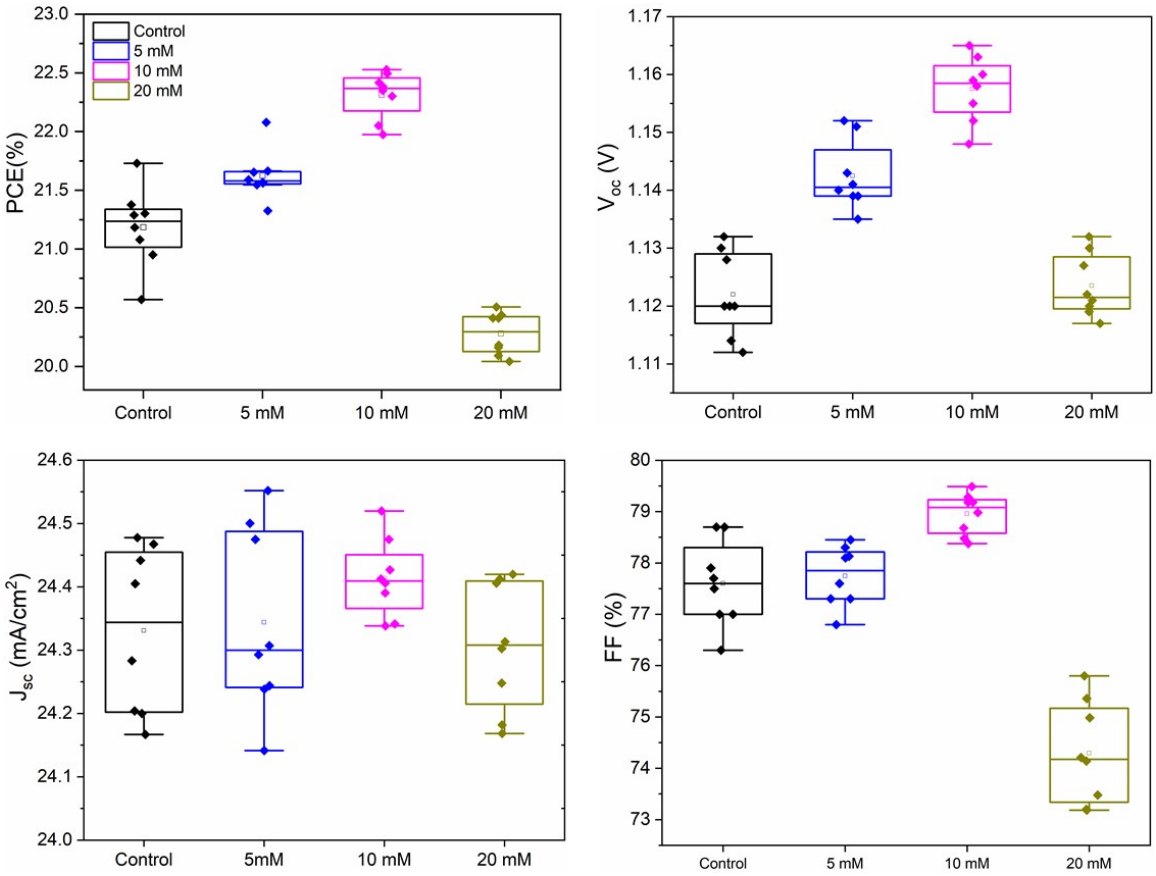

Fig. S15. Summary of photovoltaic metrics for devices with different concentration (5mM, 10mM, 20mM) of the ligand. Devices were measured without an anti-reflection coating.

Fig. S16 *J-V* curves of the champion devices under reverse scan (RS) and forward scan (FS). An antireflection coating was used.

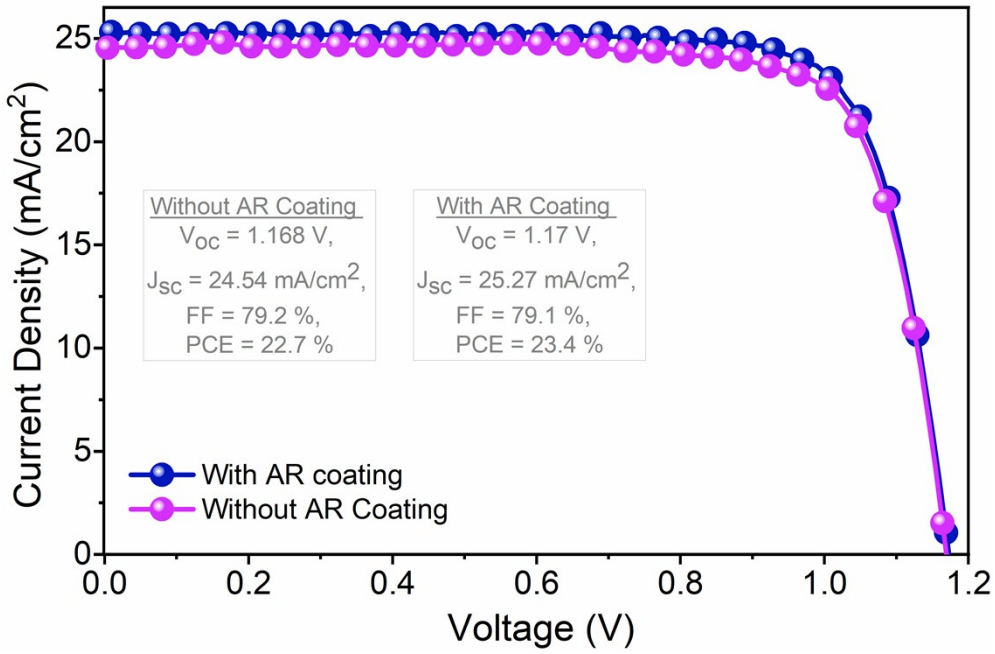

Fig. S17 J-V curve of the champion device with and without anti-reflection (AR) coating.

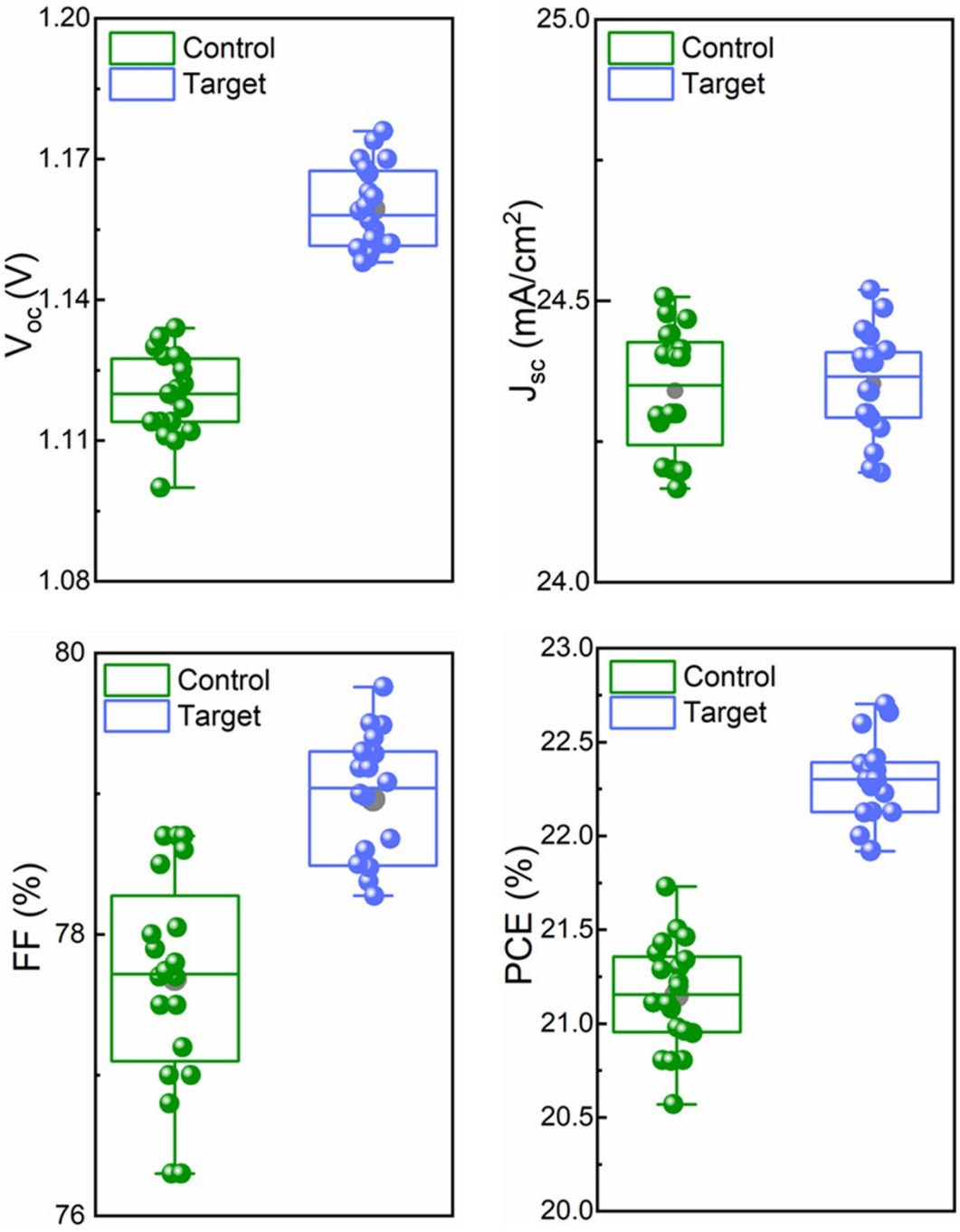

Fig. S18 Summary of photovoltaic metrics of control and target devices from two best batches Devices were measured without an anti-reflection coating.

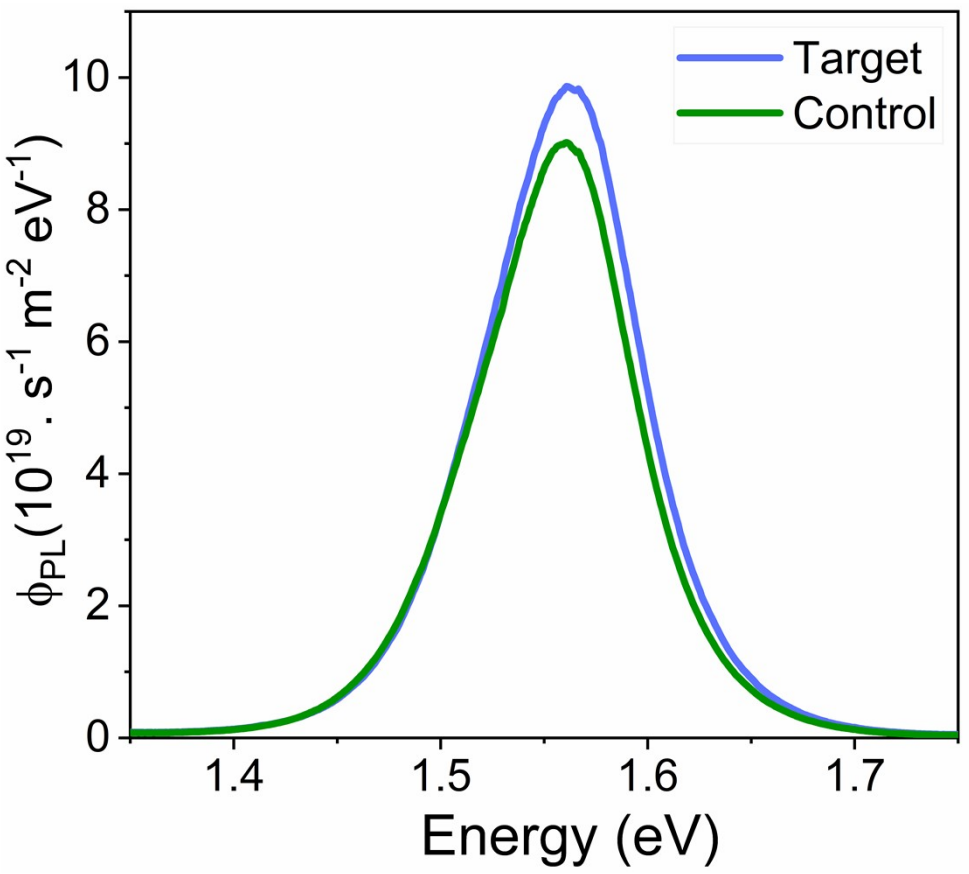

Fig. S19. Absolute photon flux $\Phi_{PL}(E)$ measurements of perovskite films at 1-sun excitation from which the PLQY is determined.

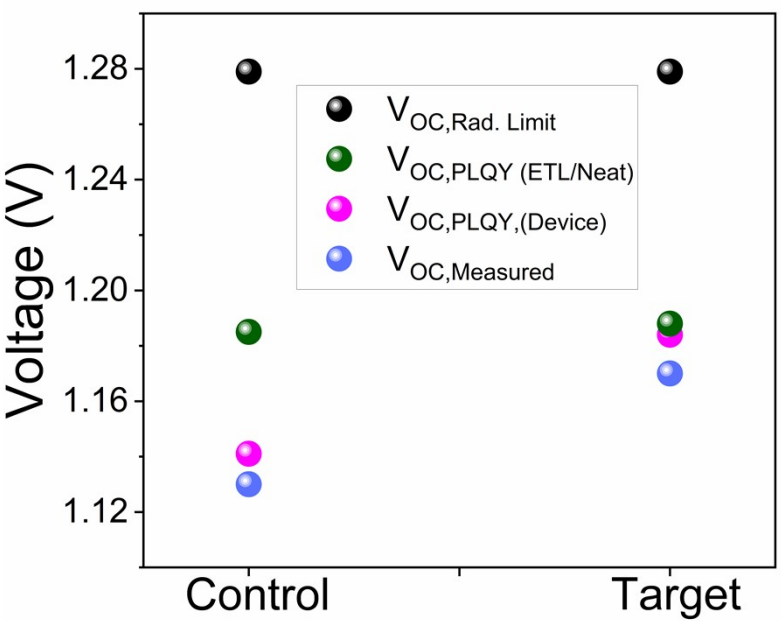

Fig. S20 V_{OC} at Radiative limit, V_{OC} at PLQY for the neat material and the full devices and V_{OC} measured for the control and target devices.

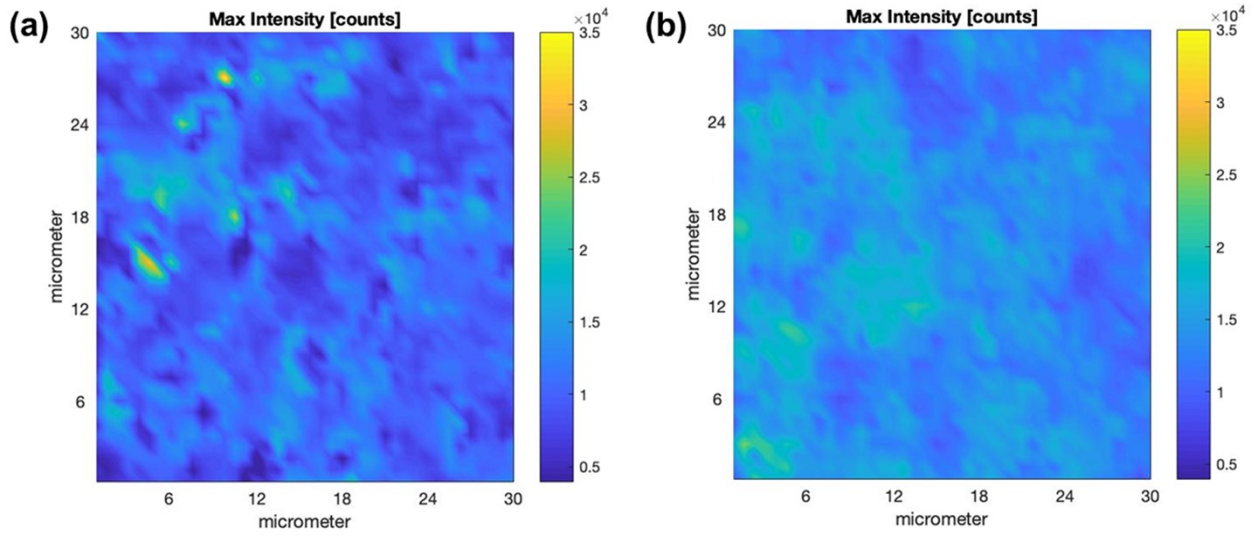

Fig. S21 PL map of a (a) control and (b) target films. Both films have architecture of FTO/TiO_2/Perovskite/spiro-OMeTAD.

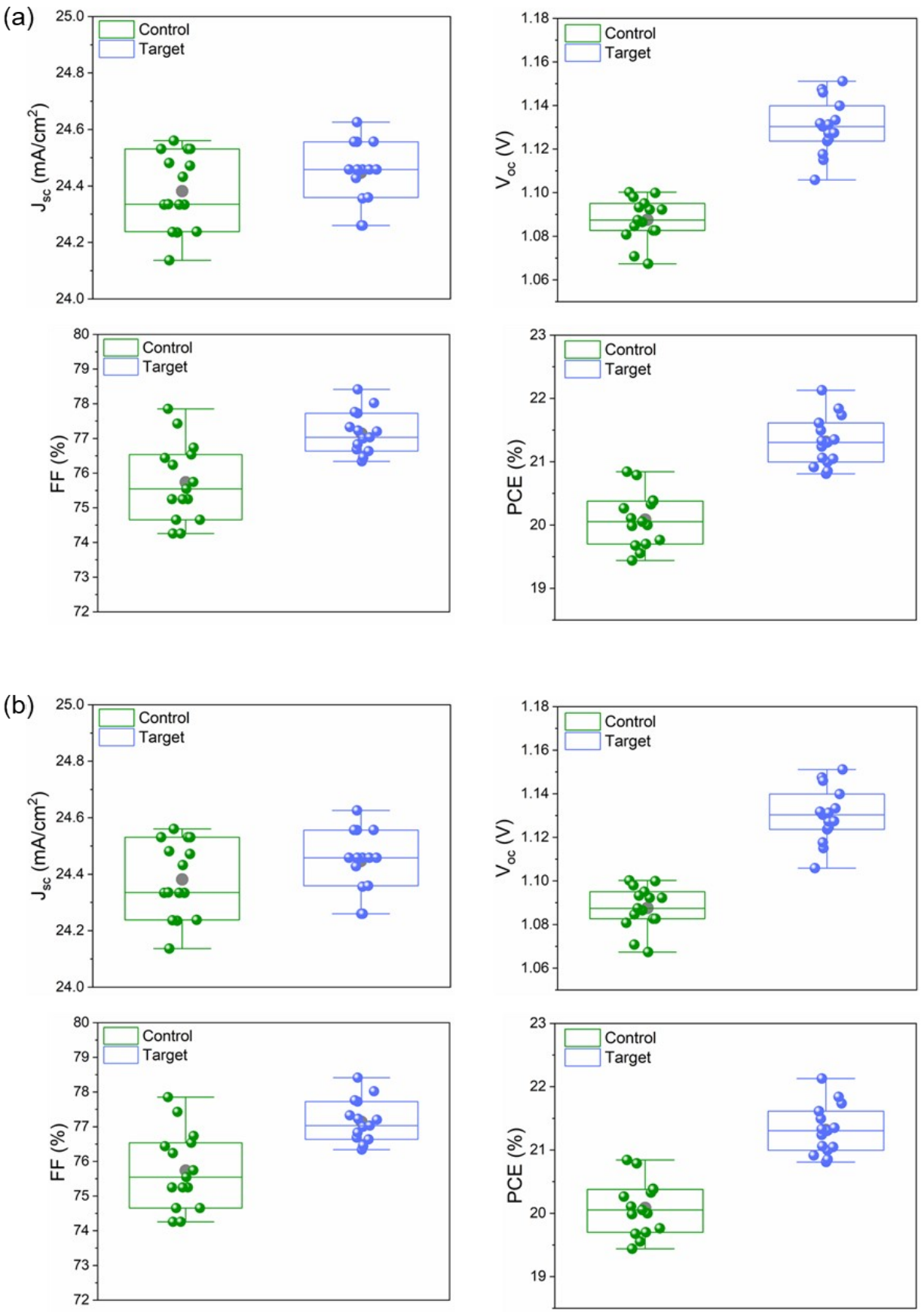

Fig. S22. (a) and (b) Statistical distribution of device parameters of the two batches of device used for stability test. Devices were measured without an anti-reflection coating.

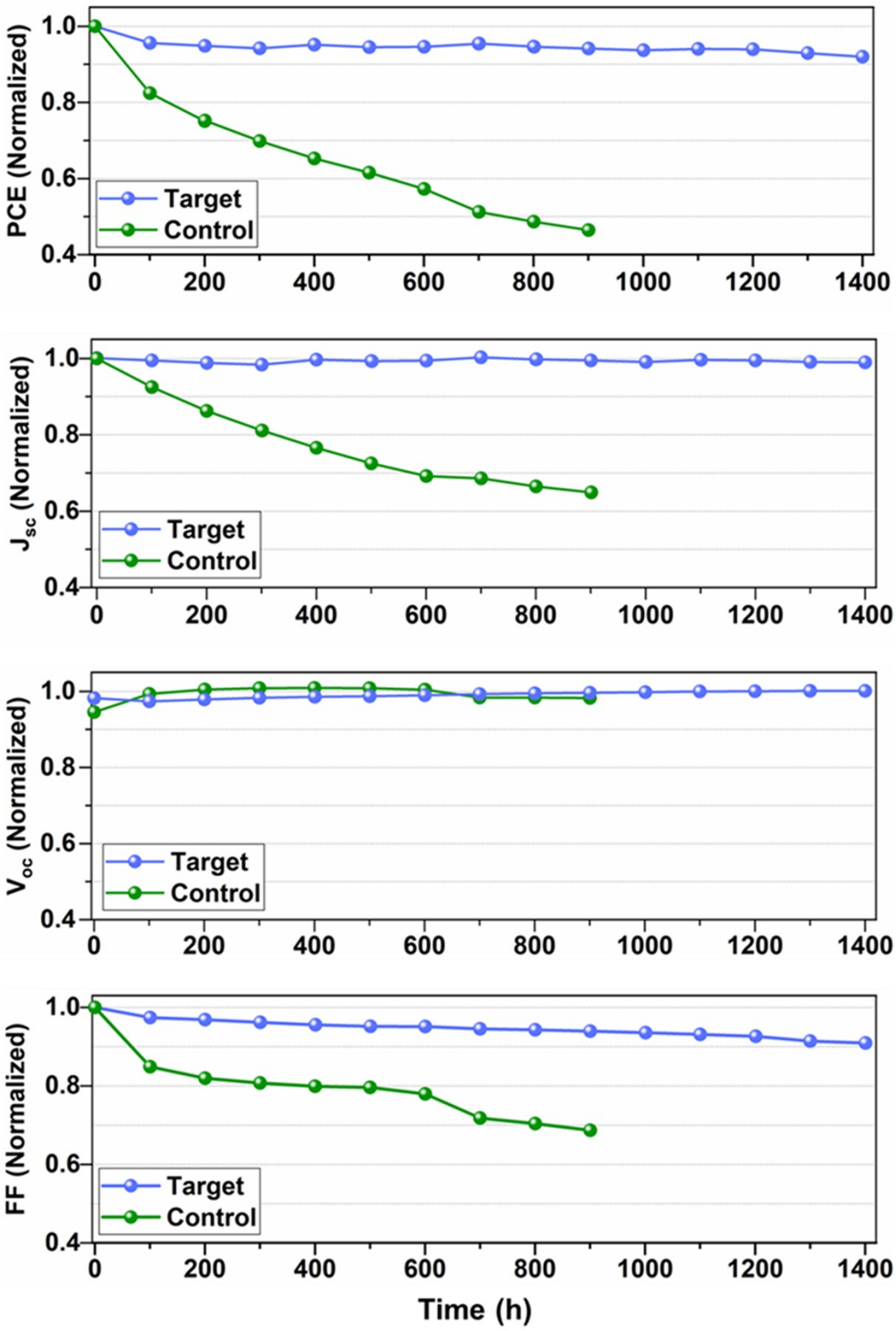

Fig. S23. The device parameter i.e., PCE, J_{SC}, Voc, and FF from the maximum power point stability test. The initial device parameters: control (PCE = 20.17 %, J_{SC} = 24.2 mAcm^2, V_{OC} = 1.094 V, FF = 76.2%) and Target (PCE = 21.0 % J_{SC} = 24.1 mA/cm^2, V_{OC} = 1.117 V, FF= 78 %).

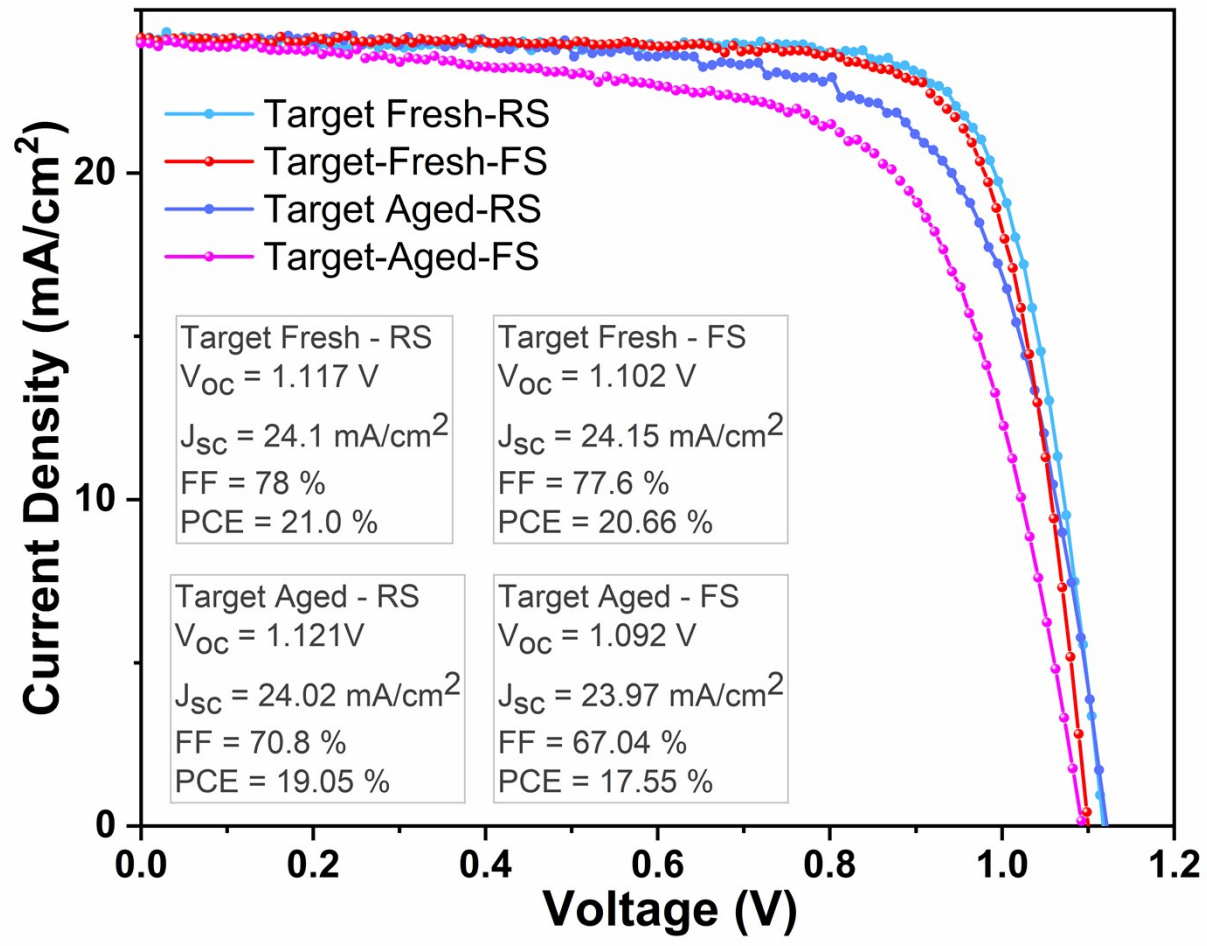

Fig. S24. The *J-V* plot of the target device before and after aging at 40 °C, 1sun at maximum power point for 1440 hours. The reserve scan (RS) and forward scan (FS) was taken at the rate of 40mV/s. Devices were measured without an anti-reflection coating.

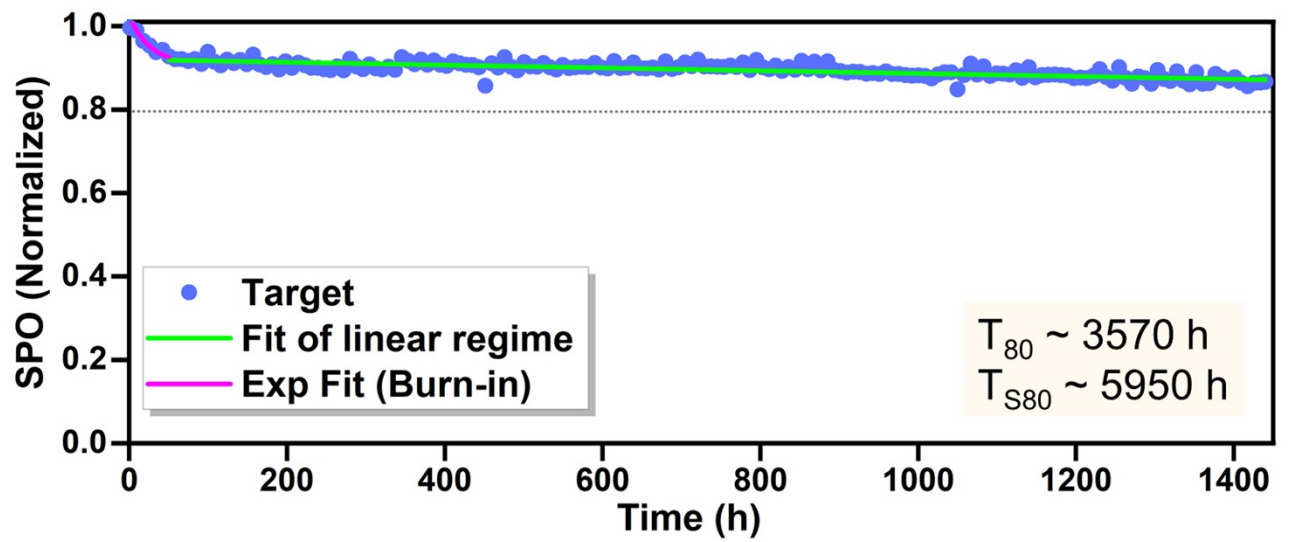

Fig. S25. The fitting of the maximum power point stability data.

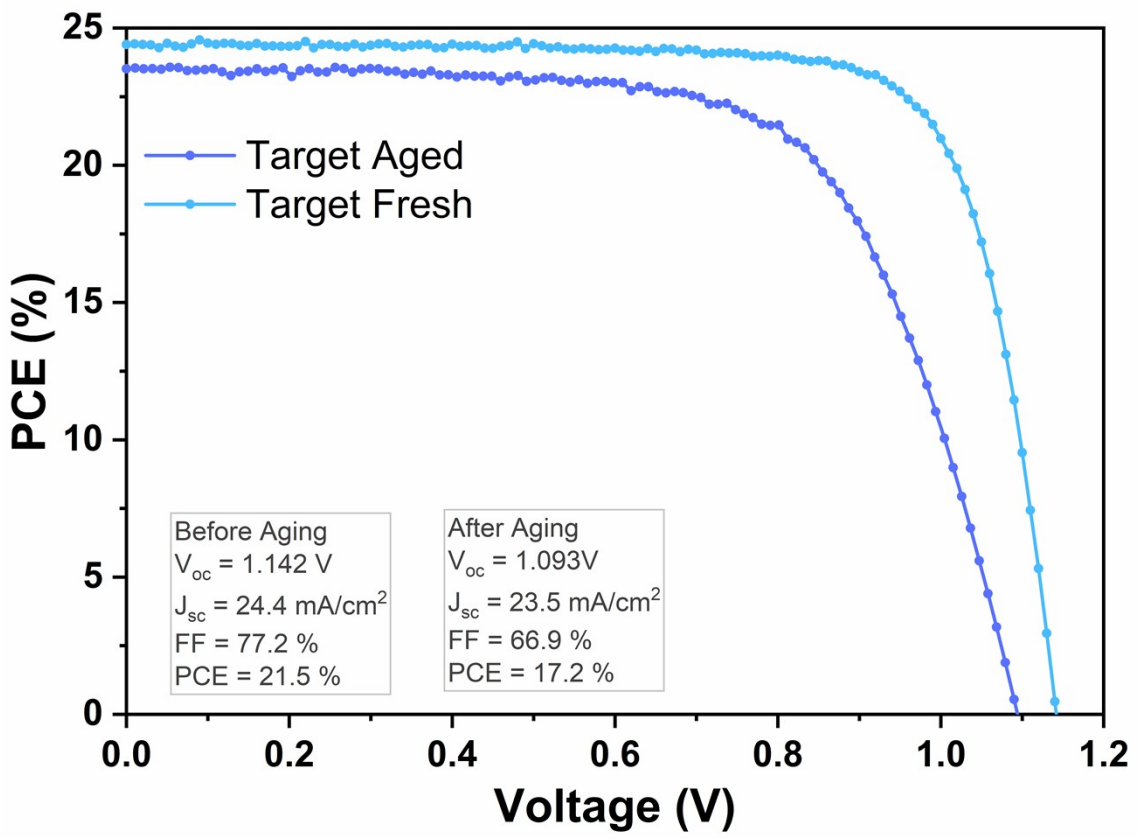

Fig. S26. The J-V plot of the target device before and after thermal aging at 85 ℃ for 1020 hours. The reverse scan was taken at the rate of 40mV/s. Devices were measured without an anti-reflection coating.

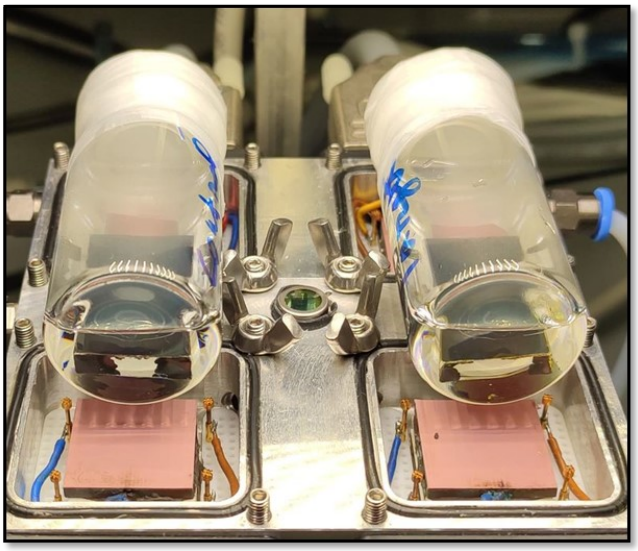

Fig. S27. The set up for the I_2 experiment.

Table S1. Summary of the photovoltaic parameters for the best control and target devices.

Device	Scan direction	V_{OC} (V)	J_{SC} (mA/cm^2)	FF (%)	PCE (%)	Stabilized PCE (%)
Control	Reverse	1.131	25.25	78.5	22.40	21.3
	Forward	1.092	25.18	73.6	20.23	
Target	Reverse	1.172	25.27	79.1	23.40	23.0
	Forward	1.156	25.22	77.8	22.68	

Table S2. Summary of the optoelectronic parameters for the control and target device.

Sample	PLQY (%)	E_{urbach} (meV)	$V_{OC.rad}$ (V)	$V_{OC, PLQY}$ (V)	$V_{OC,meas.}$ (V)
Control Film	3.19	14.1	1.274	1.185	~1.13
Control Device	0.50	14.1	1.279	1.141	
Target Film	3.17	14.4	1.277	1.188	~1.17
Target Device	2.55	14.2	1.279	1.184	

Table S3. Comparison of some of the highest long-term operational stability (MPP tracking ≥1000 h) reported in the literature for the perovskite solar cells based on n-i-p (mesoporous and planar) structure. T_{80} and T_{95} is the time where device retains 80% and 95 % of the initial PCE. Loss (%) is the [(Initial PCE – Final PCE) /Initial PCE]*100. N/A stands for not applicable and it means the data was not reported in the manuscript.

Device architecture	Aging condition	Aging Time (h)	Initial PCE (%)	Final PCE (%)	Loss (%)	Estimated T_{80} or T_{95} (h)	Reference
n-i-p mesoporous structure							
FTO/c-TiO_2/mp-TiO_2/ Perovskite/Spiro-OMeTAD/Au (Unencapsulated)	MPP, 1 Sun, 40˚C, N_2	1440	~21 %	~18.3	~13	T_{80} ~ 3570	This work
FTO/ c-TiO_2/mp-TiO_2/perovskite/spiro-OMeTAD/Au (Unencapsulated)	MPP, 1 Sun, 60˚C, Ar	1100	~ 17.14	13.71	~ 21	N/A	Nature Energy (2017)[6]
FTO/c-TiO_2/Li-doped/mp-TiO_2/ Perovskite/CuSCN/r-GO/Au (Unencapsulated)	MPP, 1 Sun, 60˚C, N_2	1000	N/A	N/A	~5	N/A	Science (2017)[7]
FTO/d-TiO_2/mp-TiO_2/ Perovskite/WBH/P3HT/Au (encapsulated)	MPP, 1 Sun, RT, RH 30%, air	1370	N/A	N/A	~5	T_{95} ~1370	Nature (2019)[8]
n-i-p planar structure							
FTO/SnO_2/pero/EH44/ MoO_x/Al (unencapsulated)	MPP, 0.77 Sun, ~30 ℃ air, RH ~10-20%,	1000	~ 12.2	~10.7	~12	N/A	Nature Energy (2020)[9]
ITO/SnO_2/PCBM:PMMA/ perovskite/PMMA/HTM /Au (Unencapsulated)	MPP, 1 Sun, 20˚C, N_2	1000	~ 19.54	~ 15.24	~22	N/A	Science (2018)[10]
ITO/SnO_2-EDTAK/PVSK(EAMA)/spiro-OMeTAD-P3HT/Au (encapsulated)	MPP, 1 Sun, RT, N_2	2000	~ 15.8	13.6	~14	T_{80} ~ 2680	Nature Energy (2020)[11]
ITO/SnO_2/1D-3D crosslinked perovskite layer/spiro-OMeTAD/Au (Unencapsulated)	MPP, 1 Sun, 25˚C, N_2	3055	~ 18.90	~ 17.58	~7	N/A	Energy Environ. Sci. (2020)[12]
ITO/SnO_2/perovskite/SEB/Au (Unencapsulated)	MPP, 1 Sun, RT, N_2	2000	~23	~ 22.3	~3	N/A	Joule (2021)[13]

References

1 I. Schnell, A. Lupulescu, S. Hafner, D. E. Demco and H. W. Spiess, *J. Magn. Reson.*, 1998, **133**, 61–69.

2 R. T. Ross, *J. Chem. Phys.*, 1967, **46**, 4590–4593.

3 U. Rau, *Phys. Rev. B - Condens. Matter Mater. Phys.*, 2007, **76**, 1–8.

4 P. Wurfel, *J. Phys. C Solid State Phys.*, 1982, **15**, 3967–3985.

5 T. Kirchartz, J. A. Márquez, M. Stolterfoht and T. Unold, *Adv. Energy Mater.*, 2020, **10**, 1904134.

6 A. D. Jodlowski, C. Roldán-Carmona, G. Grancini, M. Salado, M. Ralaiarisoa, S. Ahmad, N. Koch, L. Camacho, G. de Miguel and M. K. Nazeeruddin, Nat. Energy, 2017, **2**, 972–979.

7 N. Arora, M. I. Dar, A. Hinderhofer, N. Pellet, F. Schreiber, S. M. Zakeeruddin and M. Grätzel, Science , 2017, **358**, 768–771.

8 E. H. Jung, N. J. Jeon, E. Y. Park, C. S. Moon, T. J. Shin, T. Y. Yang, J. H. Noh and J. Seo, Nature, 2019, **567**, 511–515.

9 J. A. Christians, P. Schulz, J. S. Tinkham, T. H. Schloemer, S. P. Harvey, B. J. Tremolet De Villers, A. Sellinger, J. J. Berry and J. M. Luther, Nat. Energy, 2018, **3**, 68–74.

10 S. H. Turren-Cruz, A. Hagfeldt and M. Saliba, Science (80-.)., 2018, **362**, 449–453.

11 Z. Liu, L. Qiu, L. K. Ono, S. He, Z. Hu, M. Jiang, G. Tong, Z. Wu, Y. Jiang, D. Y. Son, Y. Dang, S. Kazaoui and Y. Qi, Nat. Energy, 2020, **5**, 596–604.

12 N. Yang, C. Zhu, Y. Chen, H. Zai, C. Wang, X. Wang, H. Wang, S. Ma, Z. Gao, X. Wang, J. Hong, Y. Bai, H. Zhou, B. Bin Cui and Q. Chen, Energy Environ. Sci., 2020, **13**, 4344–4352.

13 H. Zai, J. Su, J. Chang, H. Zai, J. Su, C. Zhu, Y. Chen, Y. Ma, P. Zhang and S. Ma, Joule, 2021, 1–16. DOI: j.joule.2021.06.00.